Finite-temperature mechanical properties of nanostructures with first-principles accuracy

L. Pizzagalli [*]

*Departement of Physics and Mechanics of Materials, Institut P', CNRS UPR 3346, Université de Poitiers, SP2MI,
Boulevard Marie et Pierre Curie, TSA 41123, 86073 Poitiers Cedex 9, France*

This paper reports an original approach allowing us to simulate the compression at finite temperature of nanostructures, based on the combination of external forces with Car-Parrinello molecular dynamics. An example of a successful application is described: the compression of buckminsterfullerene C_{60} at room temperature. It is shown that the C_{60} shell breaks at much lower strains than previously predicted, with a maximum contact force of 30 nN. This simple example demonstrates the potential of this approach, which can be especially useful to determine the mechanical properties of nanoparticles and clusters with an outstanding accuracy.

I. INTRODUCTION

Exploring materials at the nanoscale is a successful story in physics and materials science. New properties and original phenomena have thus been discovered in various domains such as phononics, plasmonics, photonics, etc. Concerning mechanical properties, an important breakthrough was achieved by using a scanning probe microscope to deform nanowires [1]. A few years later, Uchic *et al.* managed to perform the uniaxial compression of submicron pillars [2]. These works and many others led to the important result that the reduction of dimensions increases the strength [3,4]. The critical influence of size on brittleness was also demonstrated [5]. Experiments are often supplemented by classical molecular dynamics (MD) simulations [6–10]. The size dependence of strength drove investigations towards increasingly smaller nanomaterials, to discover ultrahard systems for instance [11]. Refinements and developments of alternative methods now allow for studying the plastic deformation of nanostructures with dimensions as small as a few tens of nm [12,13]. But it becomes increasingly difficult to apply deformation in a controlled manner at very low dimensions, especially for 0D systems like nanoparticles. Concerning simulations, the use of MD is questionable because classical potentials are often not reliable for small systems or large strains.

More accurate first-principles calculations could in principle be used for nanostructures with dimensions up to 3–4 nm. However a literature review reveals that the available information essentially concerns infinite 1D systems deformed at 0 K, albeit with a few exceptions [14]. In particular, it seems that the uniaxial compression at finite temperature of 0D systems with first-principles MD have never been reported. The explanation is probably that simulating an applied stress or strain on a nanoparticle is challenging. Furthermore, the strain rate must remain close to values used in classical simulations, thus requiring ion dynamics with a large number of iterations. A practical and efficient method is then needed in order to overcome both issues. In this work I describe such an approach which is built upon Car Parrinello molecular dynamics (CPMD) [15].

II. THEORY AND METHODS

A uniaxial compression could be obtained by squeezing the system to study between two slabs, thus mimicking flat punch indenter experiments. But including slabs in CPMD calculations will inflate the number of atoms excessively above a reasonable threshold. An efficient and cheapest alternative technique is to use planar repulsive force fields to replace the slabs. In the CPMD framework, such external forces can be inserted in the ionic motion equation:

$$M_\alpha \ddot{\mathbf{R}}_\alpha(t) = -\frac{\partial}{\partial \mathbf{R}_\alpha(t)} E[\{\Psi(t)\}, \mathbf{R}(t)] + \mathbf{F}_\alpha[\mathbf{R}_\alpha(t), t]. \quad (1)$$

$E[\{\Psi(t)\}, \mathbf{R}(t)]$ is the total energy of the nanostructure, as in the original CPMD equation [15]. $\mathbf{F}_\alpha[\mathbf{R}_\alpha(t), t]$ is a time dependent external ionic force acting on ion α. It is decomposed into parallel and perpendicular components relative to the chosen compression axis:

$$F_\alpha^\parallel = -\xi_u K\left(R_\alpha^\parallel - \lambda_u\right)^2 + \xi_d K\left(R_\alpha^\parallel - \lambda_d\right)^2 \quad (2)$$

$$F_\alpha^\perp = (\xi_u + \xi_d)\,\Gamma M_\alpha \dot{R}_\alpha^\perp \quad (3)$$

$$\xi_u = H(R_\alpha^\parallel - \lambda_u) \quad (4)$$

$$\xi_d = H(\lambda_d - R_\alpha^\parallel). \quad (5)$$

Equation (2) sets the repulsive forces producing mechanical compression. $F_\alpha^\parallel$ depends on the α ion position relative to two planes perpendicular to the compression axis and defined by positions λ_u and λ_d ($\lambda_u > \lambda_d$). The functions ξ_u and ξ_d determine whether the force is applied or not on ion α through the use of the Heaviside function H [Eqs. (4) and (5)]. Practically, the α ion will be repelled if its coordinate along the compression axis becomes greater than the up plane position (λ_u) or lower than the down plane (λ_d). The repulsion strength is prescribed by the constant K. A time dependent

*laurent.pizzagalli@univ-poitiers.fr

compression is obtained by setting $\lambda_u(t) = -vt + \lambda_u(t_0)$ and $\lambda_d(t) = vt + \lambda_d(t_0)$, with v a constant velocity. Finally, $F_\alpha^\perp$ is a friction force, the utility of which will appear in the following. It is only exerted on ions for which $F_\alpha^\parallel \neq 0$ and depends on the ion velocity parallel to the compression planes $\dot{R}_\alpha^\perp$ and the ion mass M_α [Eq. (3)]. The friction strength is set by the parameter Γ.

These additions to the original CPMD formalism allow for simulating the dynamical compression of nanostructures, with a negligible supplementary cost. They were used for investigating the mechanical properties of buckminsterfullerene C_{60} at room temperature, to demonstrate the feasibility and validity of the approach. Investigating the dynamical compression of C_{60} has also scientific merits. In fact, the available information from classical MD and tight-binding calculations suggests that the structural integrity of C_{60} is preserved even at compression strains exceeding 66% [16–19]. As will be revealed here, this is probably overestimated. Another issue is the lack of quantitative data in these studies, due to the methodology used to deform C_{60}.

The calculations are performed using a modified CPMD code from the Quantum Espresso package [20]. The electronic structure calculations are performed in the framework of density functional theory, with a plane wave cutoff of 25 Ry (200 Ry) for wave functions (charge density), the PBE exchange correlation functional [21], and an ultrasoft pseudopotential [22]. A $(20 \text{ Å})^3$ supercell is used, ensuring no spurious periodic interactions even when C_{60} is highly compressed. With these parameters, the bond lengths in the minimum energy structure are 1.401 and 1.451 Å, in excellent agreement with experiments [23].

The compression velocity in classical MD simulations is typically 0.1 Å/ps [24]. It implies hundreds of thousands of iterations, i.e., it is a challenging task for CPMD calculations. Extensive testing was then made to optimize dynamics parameters, yielding 600 a.u. for the effective electron mass and 5 Ry for the electron mass cutoff [25], and 0.2 fs for the timestep. The ionic temperature is controlled at 300 K by using a Nose-Hoover thermostat with an oscillation frequency of 30 THz. The compression is obtained by moving the two planes defined above towards each other with a velocity $v = 0.05$ Å/ps, corresponding to a compression speed of 0.1 Å/ps. The repulsion strength K is set to 30 a.u.

Initial compression simulations revealed two important issues. First, it is needed to control the temperature of the fictitious electrons in order to preserve the adiabatic decoupling with ions. A Nose-Hoover thermostat is then also used for electronic degrees of freedom, with an electronic kinetic energy target of 0.005 u.a. and an oscillation frequency of 90 THz. The second issue concerns the frequent observation of C_{60} rotation during compression. It seems to be initiated by small orientation change of the molecule with respect to compression axis, and the rotation speed tends to increase over time. As a consequence, the ion velocities do not sample a canonical distribution at the targeted temperature despite the use of the thermostat. To remedy this issue, a velocity dependent friction force is applied on repelled ions [Eq. (3)]. Depending on the friction strength Γ, the rotation of C_{60} is largely mitigated or even suppressed.
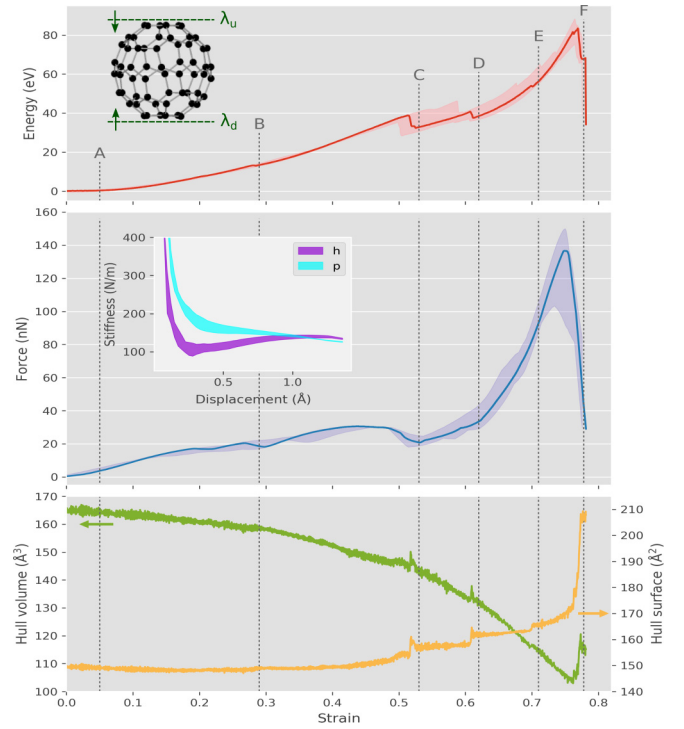

FIG. 1. Potential energy of C_{60} (top), contact force (middle, rolling average with a 0.0588 strain period), convex Hull surface and volume (bottom) of C_{60}, all quantities as a function of compression strain. Full curves correspond to a 300 K simulation with an initial h orientation and $\Gamma = 50$ a.u., whereas colored strips display the ranges built from all simulations (Table I). C_{60} configurations for strains corresponding to letters A–F are shown in Fig. 2. The inset graph shows the stiffness computed by linear interpolation of the contact force for an increasing displacement range, with colored strips built from h (violet) and p (cyan) runs (1 Å displacement equates to a strain of 0.147).

III. RESULTS

Ten different cases are investigated, with various friction strength Γ values, and two initial C_{60} orientations with respect to the compression axis, as reported in Table. I. The initial orientation corresponds to the compression axis centered on either a hexagon (h) or a pentagon (p). Γ is expressed in atomic units, i.e., here in Ha/$\hbar$. Table I also reports data obtained from the simulations. ε_1 is the strain corresponding to the C_{60} shell breaking as determined from the energy variation. ε_1^* is the same quantity but for a $10\times$ lower compression speed ($v = 0.005$ Å/ps). ε_1^F is also an elastic strain limit but determined from the force variation. Finally, ε_2 is the strain corresponding to the flattening of C_{60}, determined from the energy variation. The last row of Table I gives the average for each quantity with the standard deviation between parentheses.

Figure 1 shows the variations during compression of several quantities for an orientation h and $\Gamma = 50$ a.u.: the C_{60} potential energy, the contact force, and the surface and volume of C_{60} as determined from a convex Hull calculation. The contact force is the average of nonzero repulsion forces [Eq. (2)] for top and bottom compression planes (raw data, as well as estimations of contact surfaces and stresses, are shown in

TABLE I. Parameters used for the calculation of investigated cases and extracted data from the results. See text for explanations.

Run (#)	Orientation	Γ (a.u.)	ε_1	ε_1^*	ε_1^F	ε_2
1	h	50	0.514	0.500	0.48	0.769
2	h	50	0.536	0.510	0.48	0.770
3	h	0	0.496	0.492	0.48	0.762
4	h	1	0.495	0.498	0.48	0.765
5	h	5	0.505		0.48	0.760
6	h	500	0.500	0.487	0.48	0.770
7	p	50	0.587	0.505	0.49	0.772
8	p	50	0.563	0.512	0.48	0.789
9	p	0	0.500	0.491	0.49	0.763
10	p	500	0.530	0.533	0.49	0.770
Mean (std)			0.523 (0.030)	0.503 (0.013)	0.483 (0.005)	0.769 (0.008)

Fig. S1 [26]). The letters mark different compression steps, with the corresponding C_{60} geometries shown in Fig. 2. The full sequence can be visualized in a movie [26].

At A, C_{60} is barely deformed with imperceptible surface and volume changes (Fig. 2 A). The energy and force increase quadratically and linearly, respectively, as expected for an elastic deformation. No attempts were made to determine a Young modulus which is not well defined for a compressed system with a spherical symmetry, due to nonuniform internal strains and ill-defined C_{60} shell thickness [27]. Instead, the second order stiffness is determined from linear regression of the contact force, for increasing displacement ranges (Fig. 1). It is overestimated for small displacement ranges below about 0.1 Å because of thermal oscillations, but converges to 130–140 N/m at 1 Å. This is significantly smaller than the graphene value [28] but similar to measurements made on large hollow BN nanospheres [29]. Unexpectedly, it is also found that the stiffness depends on the orientation in the range 0.2–0.8 Å, a p orientation being stiffer than the h one. A similar orientation dependence of stiffness was obtained using atomic force microscopy on a single C_{60} [30].

Although the energy variation is monotonic up to B, it is not the case for the force curve (Fig. 1). Small decreases are associated with changes in the C_{60} orientation with respect to the compression axis. In the displayed case, the compression, initially h, becomes centered on a pentagon at B. These realignments are observed in most runs, except for the largest friction strength values, and usually leave the C_{60} in a p oriented state. During this stage, the C_{60} volume decreases mainly because of the flattening of compressed edges (Fig. 2 B), with negligible surface area changes.

It is found that the rupture of the C_{60} shell is initiated by the breaking of usually two bonds, on the lateral side of the molecule. Those are stretched by the lateral expansion of C_{60} induced by vertical compression. However, which bond breaks is purely stochastic, yielding various possible configurations of broken C_{60}. Figure 3 shows a selection of geometries obtained in the calculations.

Significant energy and force drops, correlated with spikes on volume and surface curves, are observed just before C (Fig. 1). They occur for strains of about 0.5 in all runs. In the displayed case, they are associated with the breaking of two adjacent bonds on the C_{60} lateral side (Fig. 2 C). No coordination defects remain due to reconstruction. A structural

analysis of the 10 runs allows for identifying seven different configurations (see Fig. 3 for selected examples). All these structures result from the breaking of at least two bonds, which were severely stretched by the lateral expansion due to the vertical compression. However, which bond break is a purely stochastic event, yielding various possible configurations of broken C_{60}. It is noteworthy that this result contradicts previous investigations based on classical MD calculations, for which no bond breaking was reported [16,18,31].

To confirm this point, the compression of C_{60} was performed using classical MD calculations and several interatomic potentials. It is found that the breaking of the C_{60} shell occurs for strains of at least 0.77 using REBO [32], Tersoff [33], and AIREBO [34], i.e., much greater than with CPMD. The GAP potential [35] performs better, but the critical strain of 0.60 remains largely overestimated. Besides, the analysis of energy, contact forces, and C_{60} geometrical properties reveals significant differences with the DFT calculations for all potentials. This discrepancy illustrates the real benefit of using first-principles calculations for studying mechanical properties of nanostructures.

These sharp decreases when bonds break tend to suggest that the potential energy may be a good quantity to determine the maximum elastic strain. The range of energy variations from all runs is shown in Fig. 1. The strains corresponding to C_{60} shell breaking range from 0.495 to 0.587, with no apparent influence of initial orientation and friction strength (Table I). A possible cause for such a large range is the use of high strain rates in simulations. This issue was tested by performing additional CPMD runs with a lower compression speed $v = 0.01$ Å/ps and strains in the range 0.45–0.55. The C_{60} shell failure is observed with bond breaking mechanisms similar to the previous ones. However, the range of critical strain is now largely reduced to 0.487–0.533 (Table I). This confirms the stochastic character of the failure mechanism. Interestingly, it is found that the contact force is an even better quantity to identify the C_{60} shell breaking. In fact, all force curves are characterized by a 30 nN plateau starting at a strain of about 0.44 (Fig. 1, and Fig. S2 in Ref. [26]). The end of the plateau characterizes the initiation of C_{60} shell rupture and corresponds to an average critical strain of 0.483 with an impressively low standard deviation of 0.005 (Table I). This confirms that the compression orientation and friction strength have little influence on C_{60} shell failure (see Fig. S2
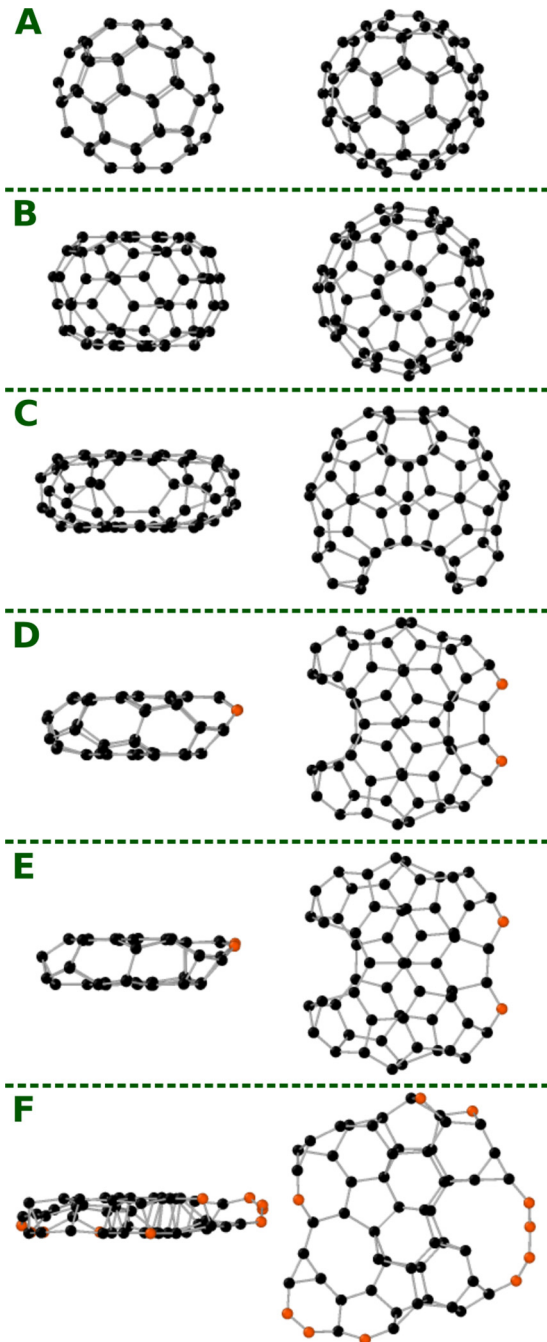
FIG. 2. Side (left) and top (right) views of C_{60} for different compression strains: 0.050 (A), 0.290 (B), 0.530 (C), 0.620 (D), 0.710 (E), 0.778 (F) (h initial orientation, $\Gamma = 50$ a.u.). Atoms are colored according to their coordination estimated using a distance criterion of 1.81 Å.

FIG. 3. Examples of compressed C_{60} configurations (left: side view, right: top view) at strains slightly exceeding ε_1 (see Table I). The run number is indicated for each configuration. Atoms are colored according to their coordination estimated using a distance criterion of 1.81 Å.

in Ref. [26] for an illustration). It also reveals that 30 nN is the maximum force that can be sustained by the C_{60} shell before breaking.

Another sharp decrease can be seen just before D on the energy curve in Fig. 1. It corresponds to another bond breaking followed by local reconstruction, located at the opposite side of the first created defect (Fig. 2 D). Among other investigated cases, the occurrence of these secondary events depends on the C_{60} structure after the first bonds broke. More than one
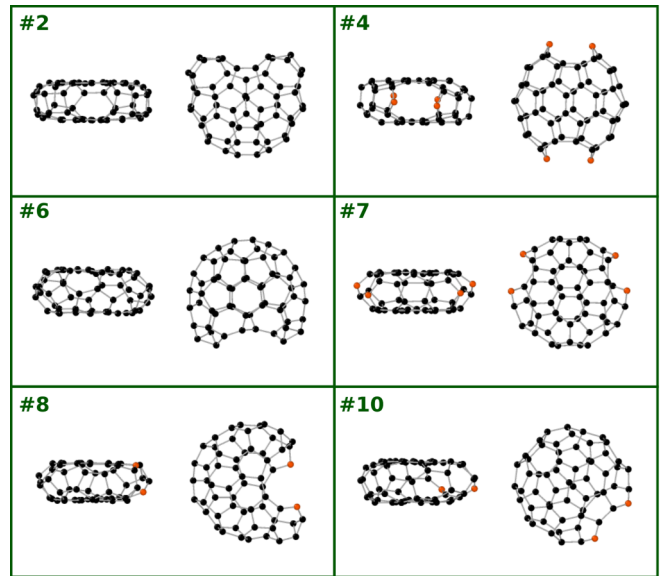
can be observed in succession or alternatively none. All bond breaking events cause a significant increase of the C_{60} Hull surface (Fig. 1).

At E, C_{60} is highly compressed and resembles two flat graphene flakes linked by a few lateral carbon atoms (Fig. 2 E). The volume is now about two thirds of its original value. Continuing the compression allows for energy and force to be as large as 90 eV and 150 nN, respectively. Large decreases corresponding to the partial transformation of the previous geometry to a 2D system are next obtained. Despite a significant pressure release, the final energy is large, due to disorder and to a large number of coordination defects (Fig. 2 F). All runs lead to different final structures. However, it is noteworthy that the critical strain for which flattening occurs is similar in all cases, with an average of 0.769 and a standard deviation of only 0.008.

IV. CONCLUSIONS

An original approach is presented which allows for calculating the mechanical properties of systems at the nanoscale, at finite temperature and with first-principles accuracy. It relies on combining Car-Parrinello molecular dynamics with external ionic force fields which reproduce flat punch indenters as in experiments. Extensive testings revealed the need to control the fictitious electrons temperature. A workaround is also proposed in order to mitigate or suppress a potential rotation of the studied system. The feasibility of the method is successfully demonstrated in the case of the compression of a buckminsterfullerene C_{60} molecule. The calculations reveal a different picture than reported in the literature. In fact it is found that the C_{60} shell structure already breaks at strains in the range 0.49–0.53, i.e., much lower than predicted from calculations with classical potentials. Note that

this elasticity threshold could be slightly overestimated due to the high strain rate associated with molecular dynamics. It is also discovered a significant difference in stiffness depending on compression orientation. However, this orientation seems to have a negligible influence on shell rupture.

This work opens the way for the theoretical determination of mechanical properties of nanoparticles at finite temperature and with DFT accuracy. Applications to materials with finite electronic gap such as clusters of C, Si, BN and their alloys should be straightforward. Other candidates could be quantum dots made of II-VI and III-V materials. Metals could also be studied using Ensemble DFT for instance [36]. Regarding system sizes, the present work intentionally focus on a small 60-atoms structure, so as to perform a lot of tests.

Nevertheless, this approach can be applied to larger nanoparticles including several hundreds of atoms. Finally, it is noteworthy that a purely repulsive force field is used here, since the intrinsic mechanical properties of C_{60} were targeted. However, one might use alternative force fields, for instance including an attractive interaction to model adhesion. Other options would be to use force fields with different spatial relations, allowing us to apply pressure spherically or cylindrically, or with a nonlinear loading rate.

[1] E. W. Wong, P. E. Sheehan, and C. M. Lieber, Science **277**, 1971 (1997).

[2] M. D. Uchic, D. M. Dinmiduk, J. N. Florando, and W. D. Nix, Science **305**, 986 (2004).

[3] A. Sharma, J. Hickman, N. Gazit, E. Rabkin, and Y. Mishin, Nat. Commun. **9**, 4102 (2018).

[4] A. Merabet, M. Texier, C. Tromas, S. Brochard, L. Pizzagalli, L. Thilly, J. Rabier, A. Talneau, Y.-M. L. Vaillant, O. Thomas, and J. Godet, Acta Mater. **161**, 54 (2018).

[5] W. W. Gerberich, J. Michler, W. M. Mook, R. Ghisleni, F. Östlund, D. D. Stauffer, and R. Ballarini, J. Mater. Res. **24**, 898 (2009).

[6] D. Mordehai, S.-W. Lee, B. Backes, D. J. Srolovitz, W. D. Nix, and E. Rabkin, Acta Mater. **59**, 5202 (2011).

[7] F. Abed El Nabi, J. Godet, S. Brochard, and L. Pizzagalli, Modell. Simul. Mater. Sci. Eng. **23**, 025010 (2015).

[8] S. Bel Haj Salah, C. Gerard, and L. Pizzagalli, Comput. Mater. Sci. **129**, 273 (2017).

[9] D. Kilymis, C. Gérard, and L. Pizzagalli, Acta Mater. **164**, 560 (2019).

[10] A. M. Goryaeva, C. Fusco, M. Bugnet, and J. Amodeo, Phys. Rev. Materials **3**, 033606 (2019).

[11] T. Zhu, J. Li, S. Ogata, and S. Yip, Mater. Res. Soc. Bull. **34**, 167 (2009).

[12] I. Lahouij, F. Dassenoy, B. Vacher, K. Sinha, D. A. Brass, and M. Devine, Tribol. Lett. **53**, 91 (2014).

[13] E. Hintsala, A. Wagner, W. Gerberich, and K. Mkhoyan, Scripta Materialia **114**, 51 (2016).

[14] A. Furmanchuk, O. Isayev, T. C. Dinadayalane, and J. Leszczynski, J. Phys. Chem. C **115**, 12283 (2011).

[15] R. Car and M. Parrinello, Phys. Rev. Lett. **55**, 2471 (1985).

[16] D. Brenner, J. Harrison, C. White, and R. Colton, Thin Solid Films **206**, 220 (1991).

[17] G. Galli and F. Mauri, Phys. Rev. Lett. **73**, 3471 (1994).

[18] Z. X. Zhang, Z. Y. Pan, Y. X. Wang, Z. J. Li, and Q. Wei, Mod. Phys. Lett. B **17**, 877 (2003).

[19] H. Shen, Mater. Lett. **60**, 2050 (2006).

[20] P. Giannozzi, O. Andreussi, T. Brumme, O. Bunau, M. B. Nardelli, M. Calandra, R. Car, C. Cavazzoni, D. Ceresoli, M. Cococcioni, N. Colonna, I. Carnimeo, A. D. Corso, S. de Gironcoli, P. Delugas, R. A. DiStasio, A. Ferretti, A. Floris, G. Fratesi, G. Fugallo, R. Gebauer, U. Gerstmann, F. Giustino, T. Gorni, J. Jia, M. Kawamura, H.-Y. Ko, A. Kokalj, E. Küçükbenli, M. Lazzeri, M. Marsili, N. Marzari, F. Mauri, N. L. Nguyen, H.-V. Nguyen, A. O. de-la Roza, L. Paulatto, S. Poncé, D. Rocca, R. Sabatini, B. Santra, M. Schlipf, A. P. Seitsonen, A. Smogunov, I. Timrov, T. Thonhauser, P. Umari, N. Vast, X. Wu, and S. Baroni, J. Phys.: Condens. Matter **29**, 465901 (2017).

[21] J. P. Perdew, K. Burke, and M. Ernzerhof, Phys. Rev. Lett. **77**, 3865 (1996).

[22] D. Vanderbilt, Phys. Rev. B **41**, 7892 (1990).

[23] C. S. Yannoni, P. P. Bernier, D. S. Bethune, G. Meijer, and J. R. Salem, J. Am. Chem. Soc. **113**, 3190 (1991).

[24] D. Kilymis, C. Gérard, J. Amodeo, U. Waghmare, and L. Pizzagalli, Acta Mater. **158**, 155 (2018).

[25] F. Tassone, F. Mauri, and R. Car, Phys. Rev. B **50**, 10561 (1994).

[26] See Supplemental Material at http://link.aps.org/supplemental/10.1103/PhysRevB.102.094102 for (i) an example of the raw variation of several indicators during compression, (ii) a movie showing a compression test, and (iii) a figure showing the influence of C_{60} orientation and friction strength.

[27] B. I. Yakobson and P. Avouris, in *Topics in Applied Physics* (Springer, Berlin, Heidelberg, 2001), pp. 287–327.

[28] C. Lee, X. Wei, J. W. Kysar, and J. Hone, Science **321**, 385 (2008).

[29] K. L. Firestein, D. G. Kvashnin, A. M. Kovalskii, Z. I. Popov, P. B. Sorokin, D. V. Golberg, and D. V. Shtansky, Nanoscale **10**, 8099 (2018).

[30] R. Pawlak, S. Kawai, S. Fremy, T. Glatzel, and E. Meyer, ACS Nano **5**, 6349 (2011).

[31] R. Mowrey, D. Brenner, B. Dunlap, J. Mintmire, and C. White, J. Phys. Chem. **95**, 7138 (1991).

[32] D. W. Brenner, O. A. Shenderova, J. A. Harrison, S. J. Stuart, B. Ni, and S. B. Sinnott, J. Phys.: Condens. Matter **14**, 783 (2002).

[33] J. Tersoff, Phys. Rev. B **39**, 5566 (1989).

[34] S. J. Stuart, A. B. Tutein, and J. A. Harrison, J. Chem. Phys. **112**, 6472 (2000).

[35] A. P. Bartók, M. C. Payne, R. Kondor, and G. Csányi, Phys. Rev. Lett. **104**, 136403 (2010).

[36] N. Marzari, D. Vanderbilt, and M. C. Payne, Phys. Rev. Lett. **79**, 1337 (1997).